

Morphological evolution in oxygen-induced faceting of Re($12\bar{3}1$)

Hao Wang, Wenhua Chen, and Theodore E. Madey*

Department of Physics and Astronomy, and Laboratory for Surface Modification, Rutgers, the State University of New Jersey, 136 Frelinghuysen Road, Piscataway, New Jersey 08854, USA

(Received 22 August 2006; published 22 November 2006)

We have studied oxygen-induced faceting of the atomically rough Re($12\bar{3}1$) surface by means of Auger electron spectroscopy, low energy electron diffraction, and scanning tunneling microscopy (STM). In contrast to previous faceting studies on other refractory metal surfaces, where simple morphologies of the facets were reported, we find a coverage-dependent morphological evolution of the facets ranging from long sawtooth ridges to complex structures exposing four different facets. The faceting occurs only when oxygen coverage (θ) exceeds 0.5 monolayer (ML) and the surface is annealed at ≥ 700 K. At low oxygen coverage ($0.5 \text{ ML} \leq \theta < 0.7 \text{ ML}$), the O/Re($12\bar{3}1$) surface becomes partially faceted upon annealing; further increasing of oxygen coverage ($0.7 \text{ ML} \leq \theta < 0.9 \text{ ML}$) causes the surface to become completely faceted, forming long sawtooth ridges along the $[\bar{2}113]$ direction with typical dimensions of ~ 8 nm in width and > 50 nm in length upon annealing at 1000 K. The size of the ridges grows with annealing temperature and annealing time, and the distance between the ridges is quite uniform. The two sides of each ridge have $(01\bar{1}0)$ and $(11\bar{2}1)$ orientations, and atomic-resolution STM images reveal that the edge of the ridge is atomically sharp. For $0.9 \text{ ML} \leq \theta < 1 \text{ ML}$, a third set of facets, identified as $(10\bar{1}0)$, emerges and truncates the original ridges. With the surface fully covered by oxygen ($\theta = 1 \text{ ML}$), a fourth facet ($01\bar{1}1$) also becomes prominent upon annealing. This morphological evolution is accompanied by a reduction of the average ridge length along $[\bar{2}113]$, indicating that the $(11\bar{2}1)$ facet is metastable. Our work demonstrates that even in a simple adsorbate/substrate system, the adsorbate-induced modification of the anisotropy of surface free energy can induce a complex sequence of changes in the surface morphology. The faceted Re surfaces may be model systems to study structure sensitivity in catalytic reactions, and may also provide promising templates to grow nanostructures.

DOI: [10.1103/PhysRevB.74.205426](https://doi.org/10.1103/PhysRevB.74.205426)

PACS number(s): 68.55.Jk, 61.14.Hg, 68.37.Ef, 68.43.-h

I. INTRODUCTION

It is well known that the interactions between adsorbates and substrates can enhance the anisotropy of surface free energy. As a result, a clean surface that is originally planar, when covered by adsorbates and annealed, may undergo faceting to reduce the total surface free energy.¹ The thermodynamically driven faceting process involves mass transport of a relatively large amount of atoms, and is affected by kinetic factors such as nucleation rate and diffusion rate. Atomically rough metal surfaces are major subjects for faceting studies because they generally have higher surface free energies than close-packed surfaces and are less stable against adsorbate-induced faceting. Previous studies on adsorbate-induced faceting of atomically rough surfaces focus on bcc metals, such as W(111), Mo(111), or fcc metals, such as Cu(210), Ir(210), Ni(210), and Pt(210) (Refs. 2–9); of all these surfaces, W(111) has been most thoroughly studied.^{10,11} So far, there are no simple rules to predict whether faceting will occur in an arbitrary adsorbate-substrate system, but oxygen is observed to cause faceting in a majority of cases. The morphological changes upon faceting often bring changes in surface electronic properties and surface reactivity. For example, evidence for structure sensitivity in butane hydrogenolysis¹² and acetylene surface chemistry¹³ has been found on planar and faceted Pt/W(111) and Pd/W(111) surfaces, respectively. On faceted Ir(210) surfaces, recent studies have also revealed structure sensitivity in chemical reactions such as the decomposition of acetylene and ammonia, and CO oxidation.^{14–16}

In this paper we extend the scope of our faceting studies from bcc and fcc metal surfaces to a hcp metal surface, Re($12\bar{3}1$), and report considerable richness in the morphology of oxygen-induced faceting: annealing Re($12\bar{3}1$) with different oxygen coverages reveals a morphological evolution from long sawtooth ridges, to complex structures exposing four different facets. Since Re is an important component in many catalysts,^{17–20} the faceted Re surfaces are attractive model systems to study structure sensitivity in Re-based catalytic reactions. A preliminary study has been carried out on methanol oxidation on oxygen-covered planar and faceted Re surfaces, showing differences in the reactivity of these two surfaces.²¹ The electronic properties of the planar and faceted Re surfaces were also investigated by high resolution soft x-ray photoemission spectroscopy (HRSXPS) using synchrotron radiation at National Synchrotron Light Source (NSLS) and reported elsewhere.²²

The orientation ($12\bar{3}1$) is chosen for two reasons. First, Re($12\bar{3}1$) is an atomically rough surface, and is expected to have high surface free energy relative to more close-packed Re surfaces, so there is a high probability that faceting may be induced on this surface. Re has a hcp structure with unit cell parameters $a = 2.761 \text{ \AA}$ and $c = 4.458 \text{ \AA}$ (Ref. 23); as shown in Fig. 1(a), the unreconstructed Re($12\bar{3}1$) surface has six layers of atoms exposed and the top-layer atoms show a quasi-hexagonal arrangement with only C_1 symmetry. Since for a hcp lattice there are two atoms in each primitive unit cell, the second stacking sequence of Re($12\bar{3}1$) is shown in

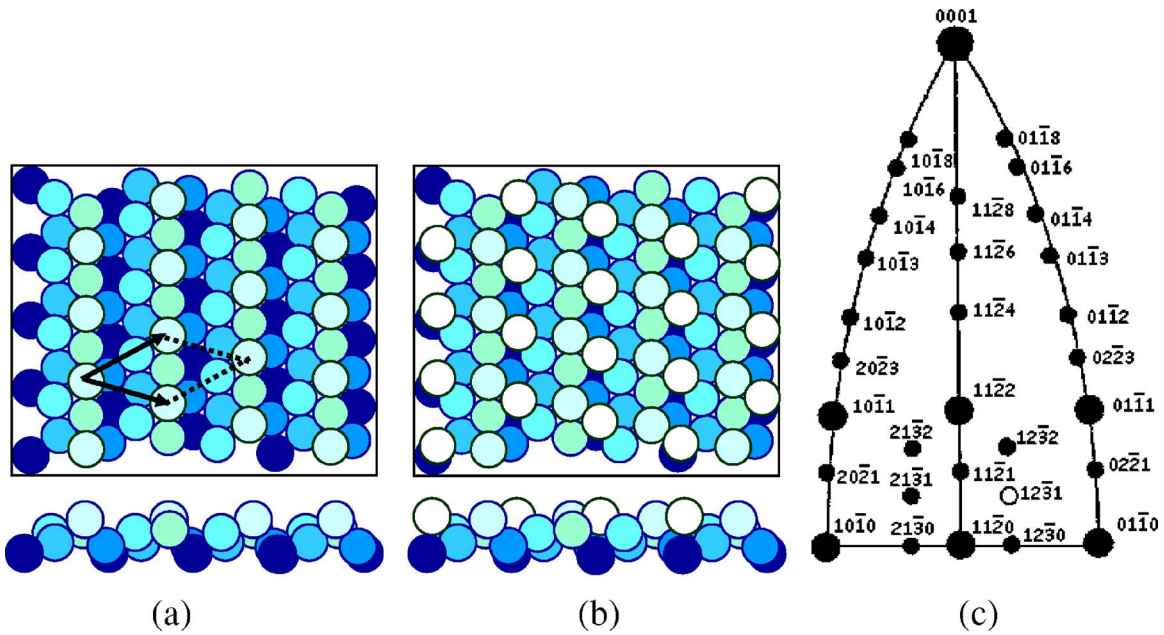


FIG. 1. (Color online) (a) A hard-sphere model of the bulk-truncated $(12\bar{3}1)$ surface with a unit cell marked. (b) The other stacking sequence of the $(12\bar{3}1)$ surface with one more layer of atoms added on top of the surface in (a). (c) The stereographic projection of the hcp lattice on the plane of $(11\bar{2}0)$. The $(12\bar{3}1)$ surface is labeled by a hollow circle.

Fig. 1(b), which has different local arrangements for the top layer atoms but the same unit cell and periodicity. Second, as shown in the stereographic projection in Fig. 1(c), the $(12\bar{3}1)$ surface is near to several more close-packed surfaces that could be potential facets, such as $(11\bar{2}0)$, $(01\bar{1}0)$, $(01\bar{1}1)$, and $(11\bar{2}2)$.

This paper is organized as follows. Section II is a brief description of the experimental procedure. In Sec. III A, we present the results of a combined study by Auger electron spectroscopy (AES), low energy electron diffraction (LEED), and scanning tunneling microscopy (STM), revealing the evolution sequence of faceting morphologies in $O/\text{Re}(12\bar{3}1)$. Section III B deals with the atomic structure of the facets, and the size dependence of facets is described in Sec. III C. A discussion of facet formation and the conclusions are given in Secs. IV and V, respectively.

II. EXPERIMENTAL

All experiments are performed in two ultra high vacuum (UHV) chambers with base pressures about 1×10^{-10} Torr. One chamber contains AES, LEED instrumentation, and a quadrupole mass spectrometer (QMS), and the other chamber contains LEED, AES, QMS, and a McAllister scanning tunneling microscope. Two $\text{Re}(12\bar{3}1)$ single crystals with a purity of 99.99% are used in the study; they are ~ 10 mm in diameter, ~ 1.5 mm thick, and aligned within 0.5° of the $(12\bar{3}1)$ orientation. The Re crystals are cleaned by cycles of e -beam heating in oxygen (1×10^{-7} Torr) followed by flashing in a vacuum to above 2000 K, and the cleanliness of the Re surfaces is checked by the AES in both chambers. The

residual contaminant species such as carbon and oxygen are below 1–2 percent of a monolayer of atoms. Oxygen is dosed on the Re surfaces at room temperature by backfilling the chamber and pressures are measured using an uncalibrated Bayard-Alpert ionization gauge. The sample temperatures are measured either by a C -type (W-5at. % Re/W-26 at. % Re) thermocouple spotwelded to the back of the Re crystal or by an infrared pyrometer. All STM measurements are made at room temperature with a typical sample bias between 0.5 to 1.2 V and a tunneling current between 0.6 and 1 nA. The X and Y dimensions of the STM scan range are calibrated using atomically resolved STM images of the $S(4 \times 4)/W(111)$ reconstruction²⁴ and the Z dimension is calibrated based on tilt angle measurements between (211) and (111) planes in faceted $O/W(111)$ (Ref. 25).

III. RESULTS

A. Morphological evolution of the facets

1. AES and LEED study

The relative oxygen coverage θ is determined from measurements of the O/Re Auger peak height ratio as a function of oxygen dose at room temperature; the oxygen dose is expressed in units of Langmuir (L, $1 \text{ L} = 1 \times 10^{-6} \text{ Torr} \cdot \text{s} = 1.33 \times 10^{-4} \text{ Pa} \cdot \text{s}$). As shown in Fig. 2, the O/Re Auger ratio increases with oxygen dose and reaches saturation when the oxygen dose is between 5 and 7 L, which is comparable with an early AES study of oxygen adsorption on a vicinal $\text{Re}(0001)$ surface, where the saturation is reached after an exposure between 7 and 8 L (Ref. 26). In a previous XPS study of oxygen adsorbed on polycrystalline Re surface, the saturation coverage is also found to be reached at an oxygen

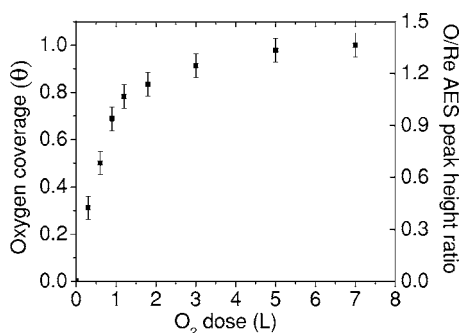


FIG. 2. The oxygen uptake curve on $\text{Re}(12\bar{3}1)$ at room temperature measured by AES. Both the O/Re Auger peak height ratio and the average O coverage (θ , in monolayers) are plotted vs O_2 dose in Langmuirs.

exposure of about 5 L (Ref. 27). If we define the coverage corresponding to the saturation O/Re Auger ratio as one monolayer (ML), i.e., $\theta = 1$ ML, the relative oxygen coverage for a given oxygen dose can be determined by normalizing the measured O/Re Auger ratio to the saturation value. This definition of saturation coverage is used here only for low oxygen doses ($< 10^2$ L) because with high oxygen doses the O/Re Auger peak height ratio may exceed the above saturation value as a consequence of surface oxidation or oxygen diffusion to the subsurface.

Figure 3(a) shows a typical LEED pattern from a clean $\text{Re}(12\bar{3}1)$ surface; all beams are characteristic of the (1×1) structure. There are no other LEED features found after annealing the surface at temperatures up to 2000 K. When the incident electron energy (E_e) increases, all the diffraction spots converge to the center of the LEED screen, indicating that the surface is macroscopically planar although it is atomically rough. No new features appear in the LEED pattern when the surface is exposed to O_2 up to 300 L at room temperature except for a slight increase of the background intensity, which can be attributed to random adsorption of oxygen atoms.

Annealing the oxygen-covered surface may cause various new features in the LEED pattern depending on oxygen exposure (coverage). When the oxygen dose is less than 0.5 L ($\theta < 0.5$ ML), the surface remains planar and retains the (1×1) structure after annealing at temperatures up to 2000 K. In contrast, when the oxygen dose is between 0.5 L and 1 L

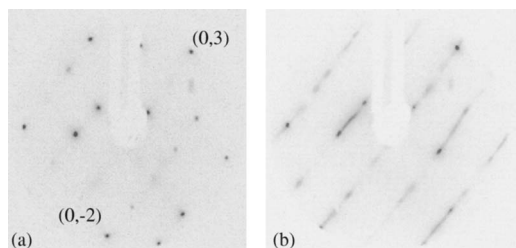


FIG. 3. (a) A LEED pattern from a clean surface with the $(0,3)$ and $(0,-2)$ diffraction spots labeled; $E_e = 70$ eV. (b) A LEED pattern from an O/Re($12\bar{3}1$) surface prepared by dosing 0.5 L O_2 ($\theta = 0.5$ ML) at 300 K followed by annealing at 900 K; $E_e = 70$ eV.

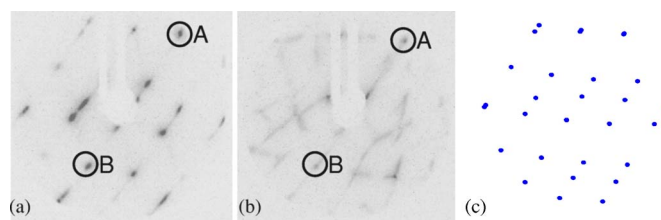


FIG. 4. (Color online) LEED patterns of a faceted O/Re($12\bar{3}1$) surface formed by dosing 3 L O_2 ($\theta = 0.9$ ML) at 300 K followed by annealing at 900 K. (a) $E_e = 70$ eV. (b) E_e varies from 40 to 146 eV. The circles A and B indicate specular beams from the facets. (c) is the kinematical simulation of (a).

($0.5 \text{ ML} \leq \theta < 0.7 \text{ ML}$), streaks along one direction emerge around the (1×1) spots after annealing at ≥ 700 K [see Fig. 3(b)]. These streaks do not converge to the screen center as E_e increases, indicating the formation of tiny facets that coexist with the $(12\bar{3}1)$ surface. For an oxygen dose between 1 L and 3 L ($0.7 \text{ ML} \leq \theta < 0.9 \text{ ML}$) and after annealing at ≥ 700 K, the (1×1) LEED spots totally disappear and the streaks in Fig. 3(b) evolve into sharp spots [see Fig. 4(a)]. Just like the streaks, these new diffraction spots do not converge to the screen center but move toward either of two fixed spots marked by two circles A and B in Fig. 4(a) when E_e increases. The two fixed spots are specular beams of the facets and this phenomenon can be better illustrated in a LEED pattern taken with variable E_e shown in Fig. 4(b), in which each short line represents the moving trace of a LEED spot as E_e is changed from 40 to 146 eV. It is clear that these lines point to the same two positions away from the center of the screen, also marked by two circles A and B, which indicates that the surface is no longer planar but completely faceted with a sawtooth ridgelike morphology.

The orientations of the two facets are determined by comparing the specular beam positions with the LEED spots from a planar $\text{Re}(12\bar{3}1)$ surface. When E_e is 70 ± 5 eV, the $(0,3)$ diffraction spot from the planar $\text{Re}(12\bar{3}1)$ surface [see Fig. 3(a)] is located almost in the same position on the LEED screen as specular beam A in Fig. 4(a) from one of the two facets; the estimated error range of E_e is due to the uncertainty of determining a perfect match and the inner potential of the Re sample. The spatial orientations of the $(0,3)$ beam can be determined simply from the structure of the reciprocal rods of $\text{Re}(12\bar{3}1)$ and the Ewald sphere construction,²⁸ from which the tilt angle between the $(0,3)$ beam and the normal direction of $(12\bar{3}1)$ is calculated as $44 \pm 2^\circ$; therefore the tilt angle of the facet relative to $(12\bar{3}1)$ is $22 \pm 1^\circ$. Similarly, a good match is found between the $(0,-2)$ spot from the planar $\text{Re}(12\bar{3}1)$ and specular beam B in Fig. 4(a) for $E_e = 85 \pm 5$ eV, and the tilt angle between this facet and $(12\bar{3}1)$ is then calculated as $12.5 \pm 0.5^\circ$. Based on these measurements, the Miller indices of the facets are identified as $(01\bar{1}0)$ and $(11\bar{2}1)$, and the ridge direction is identified as $[\bar{2}113]$. The tilt angles between $(01\bar{1}0)$, $(11\bar{2}1)$ and the substrate are 22.2° and 12.0° , respectively, agreeing well with the experimental values. Figure 4(c) shows a kinematical

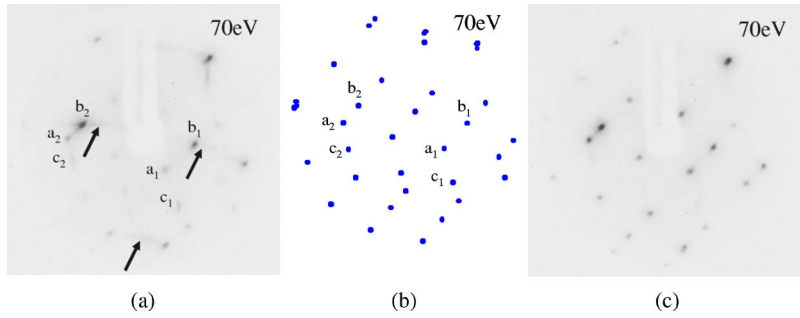


FIG. 5. (Color online) LEED patterns of faceted O/Re($1\bar{2}\bar{3}1$) surfaces formed by dosing 10 L O₂ ($\theta=1$ ML) at 300 K followed by annealing at different temperatures. (a) 1000 K, $E_e=70$ eV. (c) 1200 K, $E_e=70$ eV. (b) is the kinematical simulation of (a). See text for the labels in (a) and (b).

simulation of the faceted LEED pattern in Fig. 4(a) for $E_e=70$ eV, based on 2D lattices of bulk-truncated $(01\bar{1}0)$ and $(11\bar{2}1)$. The similarity between the simulation and the experimental pattern not only confirms the orientations of the facets but also suggests that there is no reconstruction on either of the facets, which retain their (1×1) structures.

When the oxygen dose at room temperature exceeds 3 L ($\theta\geq 0.9$ ML), the morphology of the faceted surface formed upon annealing becomes more complex with the emergence of new spots in LEED. Figure 5(a) is a typical LEED pattern from an O/Re($1\bar{2}\bar{3}1$) surface prepared by dosing 10 L O₂ ($\theta=1$ ML) followed by annealing at 1000 K. In addition to all the LEED spots from the original two facets, new faint spots [e.g. spots marked by c_1 and c_2 in Fig. 5(a)] can be seen. When E_e increases, these extra spots move toward a third direction rather than converging to either of the two original specular beam positions, indicating the formation of a third set of facets that truncate the original ridges. Since the specular beam from the third facet lies outside the LEED screen, it is difficult to determine the facet orientation directly. However, an analysis of the spatial relationship between the spots from the third facet and those from the two original facets can provide a clue. In Fig. 5(a), a_1 and b_1 mark representative spots from $(11\bar{2}1)$ and $(01\bar{1}0)$, respectively, and they form a quasi-isosceles triangle with spot c_1 , in which the distance a_1b_1 is approximately equal to a_1c_1 . When E_e changes, b_1 and c_1 move almost symmetrically relative to a_1 to retain the configuration of the quasi-isosceles triangle. The same behavior is also observed for spots a_2 , b_2 , and c_2 , where a_2 and b_2 are from $(11\bar{2}1)$ and $(01\bar{1}0)$, respectively. These observations suggest that the third facet and the $(01\bar{1}0)$ facet are spatially symmetric relative to the $(11\bar{2}1)$ facet, which leads to $(10\bar{1}0)$ as the logical choice of the orientation of the third facet [see the stereographic projection in Fig. 1(c)]. The small amount of symmetry breaking in LEED is due to the fact that the incident electron beam is along the normal direction of $(1\bar{2}\bar{3}1)$ rather than that of $(11\bar{2}1)$ and the tilt angle between these two orientations is only 12.0° . To verify this, a kinematical simulation of the LEED pattern based on 2D lattices of bulk-truncated $(11\bar{2}1)$, $(01\bar{1}0)$, and $(10\bar{1}0)$ is shown in Fig. 5(b) with spots a_1 , b_1 , c_1 , a_2 , b_2 , and c_2 labeled, which agrees well with the experimental pattern in Fig. 5(a). The tilt angle between $(10\bar{1}0)$ and $(1\bar{2}\bar{3}1)$ is 42.2° , meaning the angle between the specular

beam of $(10\bar{1}0)$ and the incident electron beam is 84.4° , which is greater than the half-maximum acceptance angle of the LEED screen (60°), and is consistent with the experimental observation that the specular beam of $(10\bar{1}0)$ lies outside of the screen. The $(10\bar{1}0)$ orientation is further confirmed in the STM study discussed in next section.

Careful examination of LEED patterns like Fig. 5(a) reveals several faint streaks marked by three arrows. These streaks do not belong to any of the three identified facets because they converge to a fourth position lying outside of the LEED screen as E_e increases. The fact that the new features are faint and streaky implies that they originate from a fourth facet that is not well developed and has limited size in one direction. For this reason, it is difficult to identify the orientation of the fourth facet from LEED. In the following section, we show how STM measurements can help provide a solution.

It is important to point out that when the oxygen dose is between 3 L and 5 L ($0.9\text{ ML}\leq\theta<1\text{ ML}$), the streaks marked by the arrows in Fig. 5(a) become less prominent. With the oxygen dose reduced to the lower limit 3 L ($\theta=0.9$ ML), the streaks disappear and only diffraction spots from $(11\bar{2}1)$, $(01\bar{1}0)$, and $(10\bar{1}0)$ can be observed. Annealing the oxygen-covered surface in Fig. 5(a) at 1200 K leads to the LEED pattern in Fig. 5(c). The streaks associated with the fourth facet disappear and the pattern looks like that from the ridges without truncation since the spots associated with the third facet are also weak. This morphology reversion can be attributed to desorption of oxygen at 1200 K (Ref. 29). By annealing at 1600 K, the coverage of oxygen remaining on the surface is not even sufficient to maintain the surface as partially faceted; the surface reverts to the planar morphology with a LEED pattern similar to Fig. 3(a).

2. STM study

Figure 6(a) shows a typical STM image from a faceted Re($1\bar{2}\bar{3}1$) surface prepared by dosing 1 L O₂ ($\theta=0.7$ ML) and annealing at 1000 K. The eye-catching feature is that the surface is not planar but completely covered by long ridges along the $[\bar{2}113]$ direction with typical length larger than 500 Å and the longest length about 1000 Å. Figure 6(b) is the cross-section profile along the line marked in Fig. 6(a), showing the sawtooth-like character of the facet morphology, from which the tilt angles of the facets relative to $(1\bar{2}\bar{3}1)$ can be determined by measuring the slopes of the line segments.

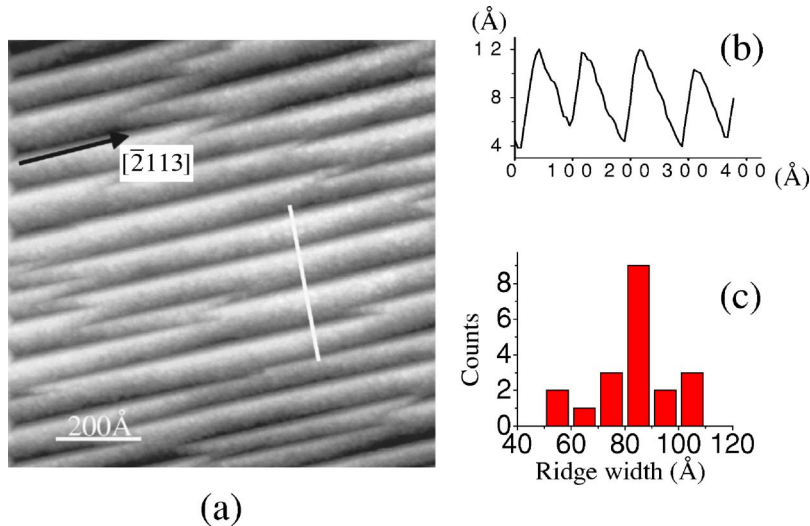


FIG. 6. (Color online) (a) STM image of a faceted $\text{O}/\text{Re}(12\bar{3}1)$ surface prepared by dosing 1 L O_2 ($\theta=0.7$ ML) at 300 K followed by annealing at 1000 K. The dimensions are $1000 \text{ \AA} \times 1000 \text{ \AA}$. (b) A cross-section profile of the line marked in (a). (c) Histogram of the ridge width distribution in (a).

Based on analysis of several similar cross-section lines, the tilt angles with respect to the substrate are measured as $23.5 \pm 1.9^\circ$ and $12.2 \pm 1.2^\circ$, respectively, which agree well with the ideal values 22.2° and 12.0° of the $(01\bar{1}0)$ and $(11\bar{2}1)$ facets identified in LEED experiments. The width of the ridges is quite uniform with a mean value $82 \pm 7 \text{ \AA}$; the result of a ridge width survey is shown in Fig. 6(c). The ridge-like morphology on the faceted $\text{Re}(12\bar{3}1)$ surface is very different from those reported to date for other refractory metal surfaces, such as $\text{W}(111)$, $\text{Mo}(111)$, and $\text{Ir}(210)$, where three-sided pyramidal facets are observed.^{8,10,30} Nevertheless, similar faceting morphology has been reported in other systems such as faceting on $\text{Pt}(210)$ induced by CO oxidation,⁹ the Ga-rich $\text{GaAs}(\bar{1}\bar{1}\bar{2})\text{B}$ surface³¹ and faceting on vicinal $\text{Si}(111)$ surfaces.³² These ridge-like structures on $\text{O}/\text{Re}(12\bar{3}1)$ are stable at room temperature; no morphological change can be found over the time span of more than a week.

As manifested in the LEED study, the STM results also reveal in greater detail that the morphology of the faceted surface depends on oxygen coverage. Figure 7(a) is a typical STM image taken from the $\text{O}/\text{Re}(12\bar{3}1)$ surface prepared by dosing 3 L O_2 ($\theta=0.9$ ML) followed by annealing at 800 K, in which the ridges are all truncated by a third set of facets as indicated by LEED measurements. Because of the large undulation of height in the ridge structure and the limited resolution of the gray scale, it is difficult to see topographic details of the facets in the raw STM images. By differentiating the height along the X direction (X slope), the details can be enhanced at the cost of losing the height information. In an X -slope STM image, regions with the same slope along the X direction are displayed with the same gray color. Figure 7(b) is the X -slope image of Fig. 7(a); this image exhibits enhanced contrast, in which the light gray areas are $(01\bar{1}0)$ facets, the gray areas are $(11\bar{2}1)$ facets, and the dark areas are attributed to the third facet $(10\bar{1}0)$. It is noteworthy that the $(11\bar{2}1)$ facets often contain bunched steps within one ridge (examples marked by small arrows), while the $(01\bar{1}0)$ facets have a much lower step density. The existence of the

steps on $(11\bar{2}1)$ is essential in the sense that ridges with one end truncated by a facet alone cannot maintain the macroscopic orientation of the original planar $(12\bar{3}1)$ substrate. If we focus on the end of one ridge shown in Fig. 7(c), the orientations of the facets identified by LEED can be further confirmed by measuring the azimuthal angles between the edge lines. The measured angle values are also shown in Fig. 7(c), which are in good agreement with the ideal values calculated from the projected intersection lines between $(11\bar{2}1)$, $(01\bar{1}0)$, and $(10\bar{1}0)$ planes on the $(12\bar{3}1)$ surface [see Fig. 7(d)].

Figure 8(a) is a typical X -slope STM image from a surface prepared by dosing 10 L O_2 ($\theta=1$ ML) and annealing at 900 K. Besides the ridges formed by $(11\bar{2}1)$ and $(01\bar{1}0)$ facets (light gray and gray areas) and truncated by $(10\bar{1}0)$ facets

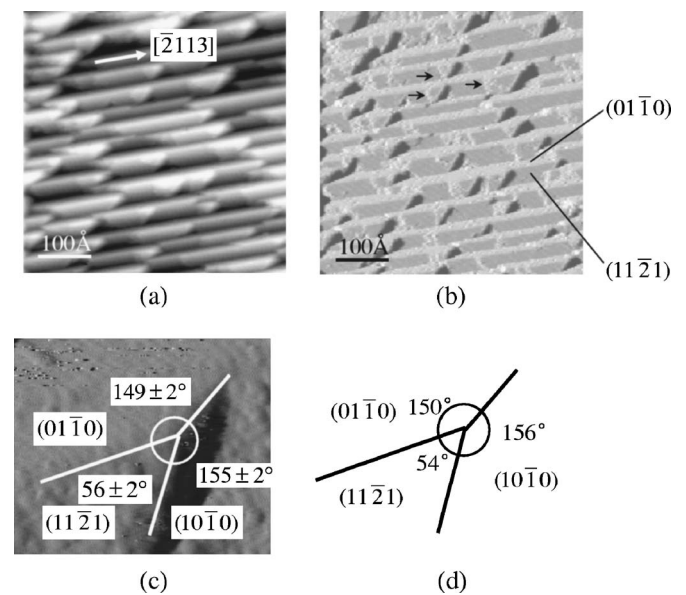


FIG. 7. STM images of faceted $\text{O}/\text{Re}(12\bar{3}1)$ surfaces prepared by dosing 3 L O_2 ($\theta=0.9$ ML) at 300 K followed by annealing at 800 K for 2 min. (a) $500 \text{ \AA} \times 500 \text{ \AA}$, raw data; (b) after the X slope taken. (c) and (d) show measured and ideal azimuthal angles of edge lines formed by facets, respectively.

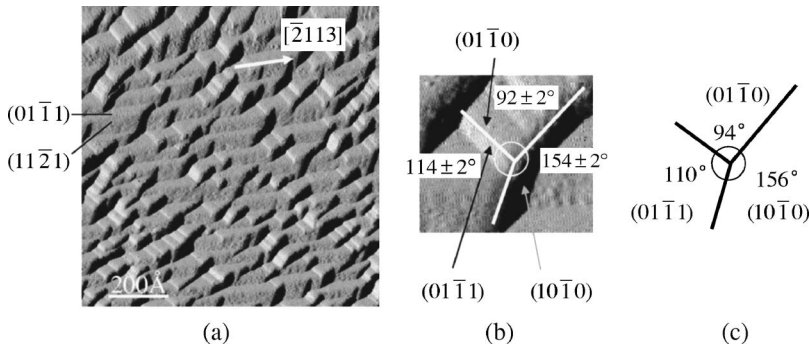


FIG. 8. (a) *X*-slope STM image of a faceted O/Re($12\bar{3}1$) surface prepared by dosing 10 L O₂ ($\theta=1$ ML) at 300 K followed by annealing at 1000 K. (b) and (c) show measured and ideal azimuthal angles of edge lines formed by facets, respectively.

(dark areas), a fourth set of facets is also prominent, as shown by bright quasirectangular areas. Most of the fourth facets have limited size in one dimension, which explains why streaks rather than sharp spots are observed from the fourth facet in LEED as previously discussed in Fig. 5(a). The fourth facet, together with ($11\bar{2}1$), ($01\bar{1}0$), and ($10\bar{1}0$) facets, can maintain the macroscopic orientation of the original planar substrate ($12\bar{3}1$). Accordingly, the bunched steps on ($11\bar{2}1$) disappear because they are not necessary to help maintain the ($12\bar{3}1$) orientation. The orientation of the fourth facet is identified as ($01\bar{1}1$) by measuring the angles between relevant edge lines. Figure 8(b) shows a typical three-sided pyramid formed by ($01\bar{1}0$), ($10\bar{1}0$) facets and the fourth facet, in which the measured angles between the edge lines are labeled. For comparison, the ideal angles between the edge lines of ($01\bar{1}0$), ($10\bar{1}0$), and ($01\bar{1}1$) facets are shown in Fig. 8(c); the small difference with the measured angle values may come from the fact that the edge lines are projected on a surface slightly deviated from the ideal ($12\bar{3}1$) surface in the measurement because the sample surface is often not perpendicular to the tip during the STM scan. A previous study on Re($01\bar{1}0$) has also found that the surface forms the ($01\bar{1}1$) facet when heated in an oxygen atmosphere.³³

B. Atomic structure of the facets

Kinematical simulations of the LEED patterns agree well with the experimental results if we assume all the facets have the ideal bulk-truncated structures. STM images with atomic resolution can provide strong support for this assumption. Figure 9(a) is an *X*-slope STM image showing the details of a two-sided faceted surface with atomic resolution: the presence of herringbone structures. On the topside of the herringbones, the stripes are continuous as marked by a double line in Fig. 9(a); the stripes correspond to the close packed atomic rows on the ($01\bar{1}0$) facet, in which individual atoms are not well resolved [see the hard sphere model in Fig. 9(c)]. On the bottom side of the herringbones, some individual atoms on the ($11\bar{2}1$) facet are resolved. In contrast to faceting on Pd/W(111), where the facet edges are truncated,³⁰ the edges along $[\bar{2}113]$ are atomically sharp. The quasi-hexagonal arrangements of the atoms on ($11\bar{2}1$) facets can be better seen in Fig. 9(b) taken from another surface

with truncated ridges. For comparison, Fig. 9(c) shows a hard-sphere model of the bulk-truncated structures of ($01\bar{1}0$) and ($11\bar{2}1$) facets projected onto ($12\bar{3}1$), in which two unit vectors of ($11\bar{2}1$) are labeled as S_1 and S_2 . The length of S_2 is also equal to the distance between atoms along $[\bar{2}113]$ in two neighboring atomic rows on the ($01\bar{1}0$) facet. The ideal lengths of S_1 and S_2 are 5.24 Å and 5.17 Å, respectively, and the corresponding values measured in Figs. 9(a) and 9(b) are 5.3 ± 0.2 Å and 5.1 ± 0.2 Å. The good agreement further confirms the conclusions drawn from the LEED study: the two sides of the ridge are ($01\bar{1}0$) and ($11\bar{2}1$), and no reconstruction occurs on these two facets.

One constraint on faceting is that the faceted structures must maintain the overall symmetry of the original planar surface.¹ In point group notation, the Re($12\bar{3}1$) surface has the lowest symmetry, C_1 . Consequently, no higher symmetry should be found in all the faceted structures. One might think that the untruncated ridges display a twofold mirror symmetry perpendicular to the ridge direction $[\bar{2}113]$. However, when one considers the atomic arrangements on the two fac-

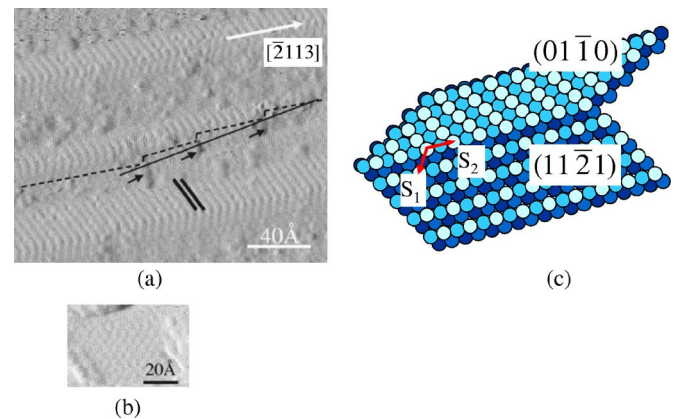


FIG. 9. (Color online) Atomically resolved *X*-slope STM images of faceted O/Re($12\bar{3}1$) surfaces prepared under different conditions. (a) The surface is prepared by dosing 1 L O₂ ($\theta=0.7$ ML) at 300 K followed by annealing at 1000 K; the dimensions of the image are $200 \text{ \AA} \times 165 \text{ \AA}$. See text for the labels. (b) The surface is prepared by dosing 10 L O₂ ($\theta=1$ ML) at 300 K followed by annealing at 1000 K; the dimensions of the image are $70 \text{ \AA} \times 50 \text{ \AA}$. (c) A hard sphere model for the two-sided faceting with two characteristic dimension parameters labeled as S_1 and S_2 .

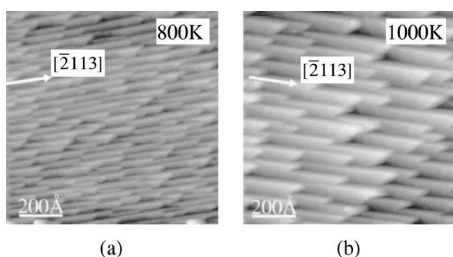


FIG. 10. $1000 \text{ \AA} \times 1000 \text{ \AA}$ STM images of faceted O/Re($12\bar{3}1$) surfaces prepared by dosing 3 L O₂ ($\theta=0.9$ ML) at 300 K followed by annealing at different temperatures for 2 min. (a) 800 K; (b) 1000 K.

ets of the ridges [see Fig. 9(c)], the mirror symmetry does not exist.

Figure 9(a) also provides insights into why the ridges that are not truncated by $(10\bar{1}0)$ facets have wedge-like terminations [see Fig. 6(a)]. The $(11\bar{2}1)$ facet shown in the middle section of Fig. 9(a) actually consists of four terraces separated by three steps marked by three arrows. The interception lines along $[\bar{2}113]$ between the terraces and the top neighboring $(01\bar{1}0)$ facet are shifted from each other by a small amount [see the dashed lines in Fig. 9(a)]. The overall envelope of the interception lines [see the solid line in Fig. 9(a)] thus shows a deviation from the $[\bar{2}113]$ direction, resulting in a wedgelike end shape for the ridge.

C. Size dependence of the facets

Faceting is a thermodynamically driven but kinetically limited process.^{1,10} Several factors control the final facet size, including coverage of the adsorbate, annealing temperature, and annealing time. For fixed oxygen coverage and annealing time, Figs. 10(a) and 10(b) show that the facet size grows as the annealing temperature increases. Similarly, for fixed oxygen coverage and annealing temperature, the facet size increases when the annealing time increases, as shown in Figs. 11(a) and 11(b). In this section, we focus on how the facet size depends on oxygen coverage. Figures 12(a)–12(c) show morphologies of the faceted surfaces prepared with different oxygen coverages ranging from 0.7 to 1 ML and the same annealing temperature ($T=800$ K) and annealing time

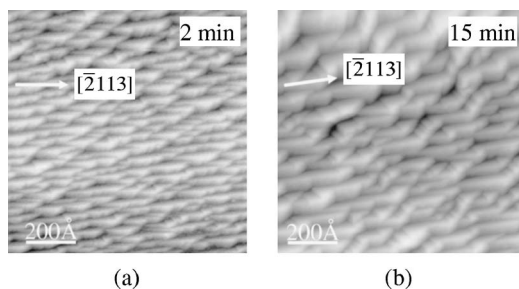


FIG. 11. $1000 \text{ \AA} \times 1000 \text{ \AA}$ STM images of faceted O/Re($12\bar{3}1$) surfaces prepared by dosing 10 L O₂ ($\theta=1$ ML) at 300 K followed by annealing at 900 K for different time. (a) 2 min; (b) 15 min.

($t=2$ min). Since for all the faceted structures, the ridges along the $[\bar{2}113]$ direction are present no matter whether they are truncated or not, we can use the ridge length and width as two characteristic quantities to describe the facet size. The histograms in Figs. 12(d)–12(f) are the ridge length distributions corresponding to the surfaces in Figs. 12(a)–12(c) and Figs. 12(g)–12(i) show the ridge width distributions, respectively. Clearly, the most probable ridge length decreases when the oxygen coverage increases. However, although the profiles of the width distributions are quite different for surfaces with different oxygen coverage, the most probable ridge width does not vary much. To better illustrate these two different trends in the ridge length and width distributions, the mean values of the ridge length and width vs oxygen coverage are plotted in Figs. 13(a) and 13(b) for two fixed annealing temperatures (800 K and 1000 K), in which the error bars show the corresponding standard deviations of the means. For any of the given oxygen coverages, both the ridge width and length increase with increasing annealing temperature. However, at the same annealing temperature, the mean ridge length decreases with increasing oxygen coverage, while the mean ridge width remains almost constant.

IV. DISCUSSION

The thermodynamical analysis of faceting is usually conducted in the context of the equilibrium crystal shape (ECS) of a small crystal with fixed volume,³⁴ and the driving force for surface faceting is the anisotropy of surface free energy. When a planar surface forms facets, all the thermally stable facets must be present in the ECS (Ref. 35), and the total surface free energy of the faceted surface $\sum_i \gamma_i A_i$ is smaller than that of the original planar surface, where γ_i is the surface free energy of facet i per unit area and A_i is the total surface area of facet i . For clean metal surfaces, the anisotropy of surface free energy is generally so small that a thermally annealed surface with relative high surface free energy [e.g., W(111), Ir(210), and Re($12\bar{3}1$)] can still retain its orientation against faceting.^{36,37} However, when the planar surface is covered by a thin layer of adsorbate atoms, the anisotropy of surface free energy can be increased to the extent that a faceted surface is more favorable energetically.

Specifically, for Re($12\bar{3}1$), if we ignore all edge energies, the energetic requirement for facet formation can be expressed

$$\sum_i \frac{\gamma_i}{\cos \theta_i} \lambda_i - \gamma_{(12\bar{3}1)} < 0, \quad (1)$$

where θ_i is the tilt angle between facet i and the $(12\bar{3}1)$ plane, and λ_i is the structural coefficient describing the partial contribution of facet i to the total projected area on $(12\bar{3}1)$ by all the facets, i.e., $\sum_i \lambda_i = 1$. Equation (1) is valid not only for a fully faceted surface but also for the coexistence of facets and the original planar surface at a steady state. From Eq. (1), the most likely facets are those having the lowest γ_i and the smallest θ_i . In general, the smoother a surface is, the smaller is the specific surface free energy. For

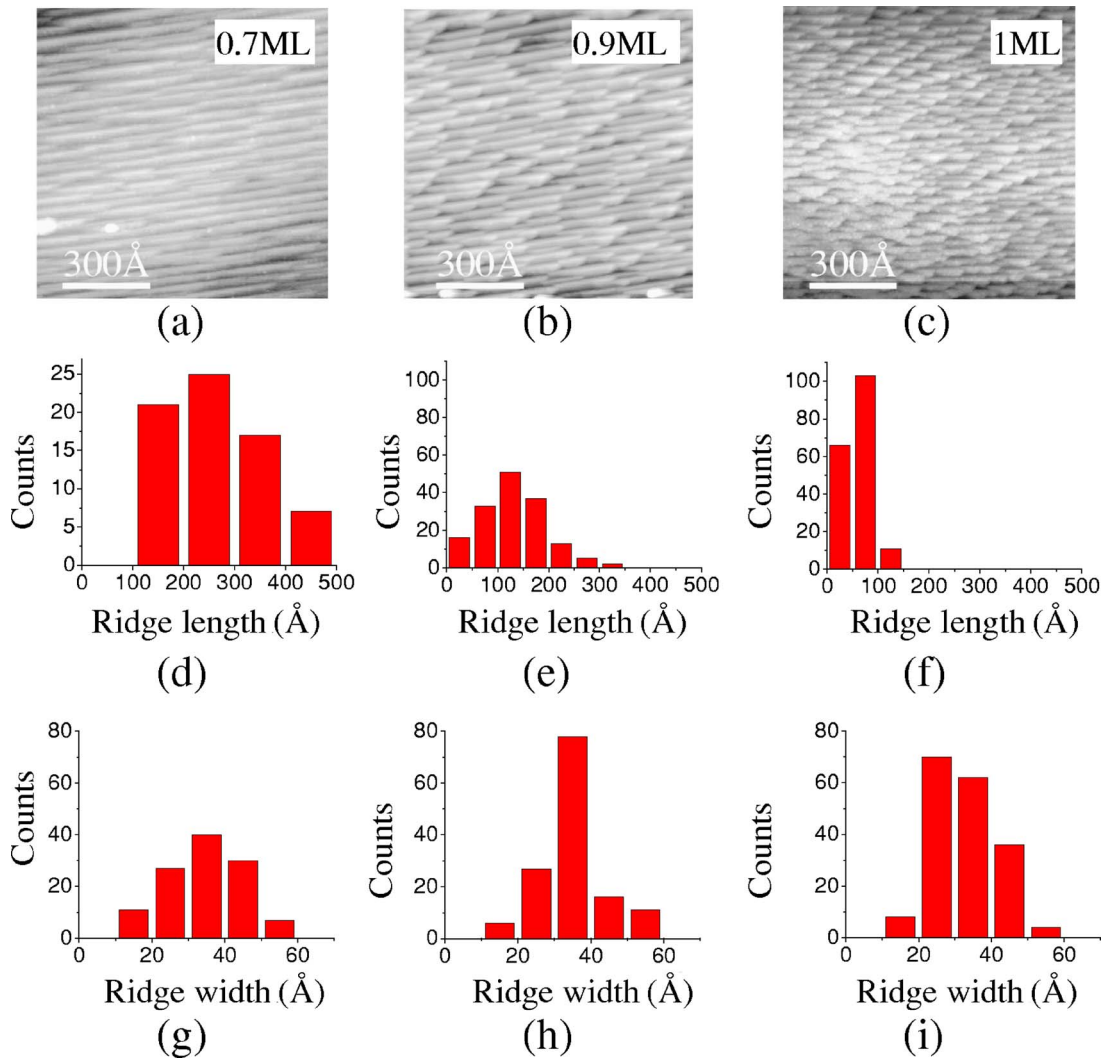


FIG. 12. (Color online) (a)–(c) are STM images of faceted O/Re($12\bar{1}$) surfaces prepared by dosing different amounts of O_2 at 300 K followed by annealing at 800 K for 2 min. The dimensions of all images are $1000 \text{ \AA} \times 1000 \text{ \AA}$. (a) 1 L, $\theta=0.7 \text{ ML}$; (b) 3 L, $\theta=0.9 \text{ ML}$; (c) 10 L, $\theta=1 \text{ ML}$. Histograms in (d)–(f) are the $[\bar{2}113]$ ridge length distributions corresponding to (a)–(c). Histograms in (g)–(i) are the $[\bar{2}113]$ ridge width distributions corresponding to (a)–(c). Only the top half region is surveyed in (c).

example, although the most close-packed (0001) surface is expected to have the lowest γ_i , its θ_i is so large (78.5°) that the increase of surface area offsets the energy gain from

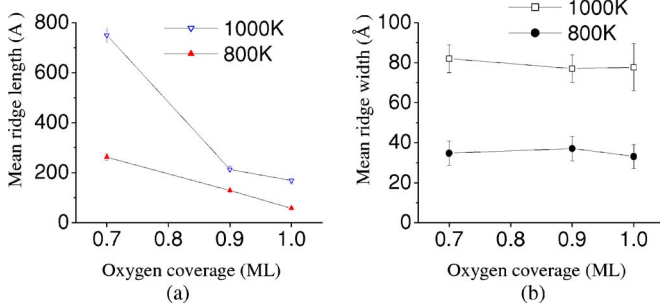


FIG. 13. (Color online) (a) Plot of mean $[\bar{2}113]$ ridge length vs oxygen coverage upon annealing at 800 K and 1000 K. (b) Plot of mean $[\bar{2}113]$ ridge width vs oxygen coverage upon annealing at 800 K and 1000 K.

reducing specific surface energy. Therefore, the (0001) orientation does not appear in the facets observed experimentally.

To predict whether a planar surface can transform into specific facets requires knowledge of γ_i , which in most cases can only be obtained from complicated electronic structure calculations.^{38–41} However, for clean metal surfaces with bulk-truncated structures, a useful qualitative comparison of γ_i can be achieved by simply counting the number of broken bonds when the bulk of a crystal is cleaved to form a surface.⁴² To a first approximation, we consider only the nearest-neighbor bonds on clean Re surfaces. Since the c/a ratio of Re is 1.615, only 1.1% smaller than that of the ideal hcp lattice (1.633), we assume the bond strength is the same for the nearest-neighbor bonds in all orientations. Based on the broken-bond counting method, the surface energies of ($12\bar{1}$) and the possible facet candidates, when they are clean, are listed in Table I together with the tilt angles between the facets and the ($12\bar{1}$) surface. We also include in

TABLE I. Specific surface energies γ_i of $(12\bar{3}1)$ and its vicinal surfaces when they are clean in the unit of broken-bond number per unit surface area. For comparison, the numerical ratios of specific surface energies between the facets and $(12\bar{3}1)$ are listed in the 3rd column. The tilt angles of the facets with respect to $(12\bar{3}1)$ are also given in both analytical and numerical forms. The last column shows the structure coefficients λ_i of facets in the simplest case: the planar $(12\bar{3}1)$ surface completely transforms into two-sided ridges composed of $(11\bar{2}1)$ and $(01\bar{1}0)$ facets.

Surface	γ_i	$\frac{\gamma_i}{\gamma_{(12\bar{3}1)}}$	$\cos \theta_i$	θ_i	$\frac{\gamma_i}{\gamma_{(12\bar{3}1)}\cos \theta_i}$	λ_i
$(12\bar{3}1)$	38	1	1	0°	1	
$(11\bar{2}1)$	$\frac{26}{a\sqrt{3a^2+28c^2}}$	1.02	$\frac{3a^2+18c^2}{\sqrt{(3a^2+28c^2)(3a^2+12c^2)}}$	12.0°	1.04	$\frac{3a^2+18c^2}{3a^2+28c^2}$
$(01\bar{1}0)$	$\frac{6}{ac}$	0.85	$\frac{5c}{\sqrt{3a^2+28c^2}}$	22.1°	0.92	$\frac{10c^2}{3a^2+28c^2}$
$(10\bar{1}0)$	$\frac{6}{ac}$	0.85	$\frac{4c}{\sqrt{3a^2+28c^2}}$	42.2°	1.15	
$(01\bar{1}1)$	$\frac{14}{a\sqrt{3a^2+4c^2}}$	0.88	$\frac{3a^2+10c^2}{\sqrt{(3a^2+28c^2)(3a^2+12c^2)}}$	24.5°	0.97	
$(11\bar{2}0)$	$\frac{4\sqrt{3}}{ac}$	0.98	$\frac{3\sqrt{3}c}{\sqrt{3a^2+28c^2}}$	15.6°	1.02	
$(11\bar{2}2)$	$\frac{14}{a\sqrt{3a^2+3c^2}}$	0.98	$\frac{\sqrt{3}(a^2+3c^2)}{\sqrt{(3a^2+28c^2)(a^2+c^2)}}$	22.7°	1.06	

Table I the structural coefficients λ_i of $(11\bar{2}1)$ and $(01\bar{1}0)$ facets for the simplest faceting case in which the $(12\bar{3}1)$ surface transforms into ridges composed of only these two facets. If we apply Eq. (1) to this simplest case assuming all the involved surfaces are clean, we have

$$\frac{\gamma_{(11\bar{2}1)}^{clean}}{\cos \theta_{(11\bar{2}1)}}\lambda_{(11\bar{2}1)} + \frac{\gamma_{(01\bar{1}0)}^{clean}}{\cos \theta_{(01\bar{1}0)}}\lambda_{(01\bar{1}0)} - \gamma_{(12\bar{3}1)}^{clean} = 0. \quad (2)$$

Therefore, a clean $\text{Re}(12\bar{3}1)$ surface does not transform spontaneously into ridges with $(11\bar{2}1)$ and $(01\bar{1}0)$ facets because there is no energy gain for such a transformation, which agrees with the experimental observation that the clean $\text{Re}(12\bar{3}1)$ surface is always thermally stable. However, upon adsorption of oxygen and annealing, the $\text{Re}(12\bar{3}1)$ surface is observed to form $(11\bar{2}1)$ and $(01\bar{1}0)$ facets; this indicates that oxygen can induce an anisotropic change of the surface free energies of $(12\bar{3}1)$, $(11\bar{2}1)$, and $(01\bar{1}0)$ so that Eq. (2) is no longer valid but Eq. (1) is fulfilled.

Generally, the adsorption of oxygen reduces the free energy of a surface; for example, the surface free energies of most metal oxides are invariably lower than those of the corresponding metal surfaces.^{38,43} More importantly, oxygen can induce enhancement of the anisotropy of surface free energy, which may be explained in terms of preferential adsorption of oxygen on certain facets. In all discussions of coverage-dependent morphology to this point, we have used the average coverage of oxygen on the planar $\text{Re}(12\bar{3}1)$ surface as the reference for comparison. When faceting occurs,

the actual oxygen coverages on different facets may be different, which, when coupled with possible different O-Re binding energies on different facets, leads to different amounts of surface energy reduction, i.e., increase of the anisotropy of surface free energy. Such an oxygen-induced enhancement of surface energy anisotropy is also observed in other systems: Avraamov *et al.* in an early experiment reported the influence of oxygen on the anisotropy of the surface free energy of silicon (3%)-iron alloy surfaces using the zero creep method;⁴⁴ recently, Walko *et al.* reported that in oxygen-induced faceting on Cu(115), the surface energy of $\{104\}$ decreases with an increase of oxygen coverage and the resulting anisotropy causes the Cu(115) surface to form both $\{104\}$ facets and stepped facets, which gradually shift to the $\{113\}$ orientation.⁴⁵

For surface faceting, a necessary condition is that the area-weighted combinations of all the facets and steps must retain the original macroscopic orientation of the planar surface, which, together with the energy requirement in Eq. (1), can give a qualitative explanation of the coverage-dependent evolution of surface morphology. Since for clean surfaces, $(01\bar{1}0)$ has the smallest γ_i and the lowest value of $\gamma_i/\cos \theta_i$ among those near $(12\bar{3}1)$, it must appear as a facet and be the major source of lowering the total surface energy if adsorbate-induced faceting ever occurs on $\text{Re}(12\bar{3}1)$. This explains why only the $(11\bar{2}1)$ facet appears with $(01\bar{1}0)$ to form ridges along $[\bar{2}113]$ at low average oxygen coverages ($0.7 \text{ ML} \leq < 0.9 \text{ ML}$), although it is rough with four layers of atoms exposed and has higher surface energy than $(12\bar{3}1)$ when both are clean (see Table I). At low average oxygen coverages ($0.7 \text{ ML} \leq \theta < 0.9 \text{ ML}$), the remaining oxygen at-

oms after preferential adsorption on $(01\bar{1}0)$ facets may not be sufficient to modify γ_i of another possible facet i significantly so that $\gamma_i/\cos\theta_i$ is probably still close to that of the clean surface listed in Table I. The $(11\bar{2}1)$ surface is the only possible choice that is close enough to $(12\bar{3}1)$ ($\theta_{(11\bar{2}1)} = 12.0^\circ$) with a medium value of $\gamma_i/\cos\theta_i$ and can retain the $(12\bar{3}1)$ orientation by forming ridges with the $(01\bar{1}0)$ facet. Other attempts to retain the $(12\bar{3}1)$ orientation are unfavorable because they either involve surfaces with higher $\gamma_i/\cos\theta_i$ to form ridges or require larger mass transport to form more complex structures. On the other hand, since the $(11\bar{2}1)$ surface is atomically rough and does not appear in the ECS of a hcp crystal,⁴² it is also a metastable phase. When the average oxygen coverage increases ($\theta > 0.9$ ML), some surface may appear as a new facet because it now has enough oxygen available to reduce γ_i so that $\gamma_i/\cos\theta_i$ becomes much less than that of $(11\bar{2}1)$. This is especially true for $(10\bar{1}0)$ since it has the same surface structure as the favored $(01\bar{1}0)$ facet and can have the same low surface energy as $\gamma_{(01\bar{1}0)}$. The total surface free energy is reduced by replacing the $(11\bar{2}1)$ facet with $(10\bar{1}0)$ that has lower γ_i , resulting in the truncation of the ridges and decrease of the average ridge length. When the $\text{Re}(12\bar{3}1)$ crystal is held at 900 K while dosing oxygen, the $(11\bar{2}1)$ facet can even disappear completely.⁴⁶

In the above discussion, the contribution of edge energy is ignored. In fact, reducing the edge energy is the dominating factor for dependence of facet size on annealing temperature and time.¹⁰ For a fully faceted surface under steady state conditions, the total surface area for each facet is fixed no matter what facet size distribution there is. No energy gain can be made by simply increasing the mean facet size. However, the edge density is reduced for bigger facet size, providing a driving force for the observed increasing of facet size at higher annealing temperature and longer annealing time. Similar phenomena have also been observed in the faceting of $\text{O}/\text{Ir}(210)$, $\text{Pd}/\text{W}(111)$, and $\text{Pt}/\text{W}(111)$ (Refs. 8, 10, and 47).

Being driven by surface thermodynamics, the faceting process is also controlled by kinetics of nucleation and surface diffusion. According to Che *et al.*,⁴⁸ when faceting occurs, there is always a nucleation barrier associated with the edge energy and the anisotropy of surface free energy; a lower barrier requires lower edge energy and larger surface energy anisotropy. That faceting on $\text{O}/\text{Re}(12\bar{3}1)$ occurs only when the annealing temperature is higher than 700 K is a manifestation that there exists such an energy barrier to over-

come toward faceting. Large facet size can be achieved by either annealing at higher temperature for shorter time or at lower temperature for longer time [see Figs. 10(b) and 11(b)]. This indicates the diffusion rate is important in determining the facet size.

V. CONCLUSIONS

We have found that the adsorption of oxygen can induce faceting of $\text{Re}(12\bar{3}1)$, and the morphology of the faceted surface depends on oxygen coverage. For oxygen coverage $\theta < 0.5$ ML, the $\text{O}/\text{Re}(12\bar{3}1)$ surface remains planar upon annealing. However, for $0.5 \text{ ML} \leq \theta < 0.7$ ML, the $\text{O}/\text{Re}(12\bar{3}1)$ surface becomes partially faceted upon annealing at ≥ 700 K. For $0.7 \text{ ML} \leq \theta < 0.9$ ML, the $\text{O}/\text{Re}(12\bar{3}1)$ surface becomes completely faceted, forming long sawtooth ridges which are composed of $(01\bar{1}0)$ and $(11\bar{2}1)$ facets upon annealing at ≥ 700 K. The distance between the ridges is quite uniform and the ridges have atomically sharp edges. For $0.9 \text{ ML} \leq \theta < 1$ ML, similar annealing treatment leads to the emergence of $(10\bar{1}0)$ facets which truncate the original ridges. With the surface fully covered by oxygen ($\theta = 1$ ML), a fourth facet $(01\bar{1}1)$ becomes prominent. This morphological evolution is accompanied by the reduction of the average ridge length along $[\bar{2}113]$, indicating that the $(11\bar{2}1)$ facet is metastable.

Our work demonstrates that even in a simple adsorbate/substrate system, the adsorbate-induced modification of the anisotropy of surface free energy can bring a complex change of the surface morphology. This complex morphological evolution is perhaps related to the low symmetry of the $\text{Re}(12\bar{3}1)$ surface, which reduces the symmetry constraint of faceted structures and leads to wider choices of facet orientations. Theoretical studies are necessary to give detailed energetic descriptions of the bonding characteristics between oxygen and Re on different facets, which, we believe, drives the change of surface energy anisotropy. Since the morphology of the faceted structures can be controlled by adjusting oxygen coverage, the faceted Re surfaces provide plausible model systems to study structure sensitivity in Re-based catalytic reactions as well as promising templates to grow nanostructures, perhaps nanowires.

ACKNOWLEDGMENTS

The authors thank A. S. Y. Chan and T. Jacob for helpful discussions. This work has been supported by the U.S. Department of Energy, Office of Basic Energy Sciences.

*Corresponding author.

Electronic address: madey@physics.rutgers.edu

¹Q. Chen and N. V. Richardson, *Prog. Surf. Sci.* **73**, 59 (2003).

²R. E. Kirby, C. S. McKee, and R. W. Roberts, *Surf. Sci.* **55**, 725

(1976).

³R. E. Kirby, C. S. McKee, and L. V. Renny, *Surf. Sci.* **97**, 457 (1980).

⁴K. Pelhos, J. B. Hannon, G. L. Kellogg, and T. E. Madey, *Surf.*

- Sci. **432**, 115 (1999).
- ⁵K. J. Song, J. C. Lin, M. Y. Lai, and Y. L. Wang, Surf. Sci. **327**, 17 (1995).
- ⁶D. B. Danko, M. Kuchowicz, and J. Kolaczewicz, Surf. Sci. **552**, 111 (2004).
- ⁷A. T. S. Wee, J. S. Foord, R. G. Egde, and J. B. Pethica, Phys. Rev. B **58**, R7548 (1998).
- ⁸I. Ermanoski, K. Pelhos, W. Chen, J. S. Quinton, and T. E. Madey, Surf. Sci. **549**, 1 (2004).
- ⁹M. Sander, R. Imbihl, R. Schuster, J. V. Barth, and G. Ertl, Surf. Sci. **271**, 159 (1992).
- ¹⁰T. E. Madey, J. Guan, C.-H. Nien, H.-S. Tao, C.-Z. Dong, and R. A. Campbell, Surf. Rev. Lett. **3**, 1315 (1996).
- ¹¹T. E. Madey, C.-H. Nien, K. Pelhos, J. J. Kolodziej, I. M. Abdelrehim, and H.-S. Tao, Surf. Sci. **438**, 191 (1999).
- ¹²R. A. Campbell, J. Guan, and T. E. Madey, Catal. Lett. **27**, 273 (1994).
- ¹³R. Barnes, I. M. Abdelrehim, and T. E. Madey, Top. Catal. **14**, 53 (2001).
- ¹⁴W. Chen, I. Ermanoski, Q. Wu, T. E. Madey, H. Hwu, and J. G. Chen, J. Phys. Chem. B **107**, 5231 (2003).
- ¹⁵W. Chen, I. Ermanoski, and T. E. Madey, J. Am. Chem. Soc. **127**, 5014 (2005).
- ¹⁶W. Chen, I. Ermanoski, T. Jacob, and T. E. Madey, Langmuir **22**, 3166 (2006).
- ¹⁷L. S. Wang, R. Ohnishi, and M. Ichikawa, J. Catal. **190**, 276 (2000).
- ¹⁸Y. Z. Yuan, H. C. Liu, H. Imoto, T. Shido, and Y. Iwasawa, J. Catal. **195**, 51 (2000).
- ¹⁹F. Solymosi, P. Tolmascov, and T. S. Zakar, J. Catal. **233**, 51 (2005).
- ²⁰K. Liu, S. C. Fung, T. C. Ho, and D. S. Rumschitzki, J. Catal. **206**, 188 (2002).
- ²¹A. S. Y. Chan, W. Chen, H. Wang, J. E. Rowe, and T. E. Madey, J. Phys. Chem. B **108**, 14643 (2004).
- ²²A. S. Y. Chan, G. K. Wertheim, H. Wang, M. D. Ulrich, J. E. Rowe, and T. E. Madey, Phys. Rev. B **72**, 035442 (2005).
- ²³D. E. Gray, *American Institute of Physics Handbook*, 3rd ed. (McGraw-Hill, New York, 1972).
- ²⁴C.-H. Nien and T. E. Madey, Surf. Sci. **433**, 254 (1999).
- ²⁵A. Szczepkiewicz, A. Ciszewski, R. Bryl, C. Oleksy, C.-H. Nien, Q. F. Wu, and T. E. Madey, Surf. Sci. **599**, 55 (2005).
- ²⁶R. Pantel and M. Bujor, Surf. Sci. **83**, 228 (1979).
- ²⁷C. Morant, L. Galan, and J. M. Sanz, Anal. Chim. Acta **297**, 179 (1994).
- ²⁸M.-C. Desjonqueres and D. Spanjaard, *Concepts in Surface Physics* (Springer-Verlag, Berlin, 1993).
- ²⁹G. K. L. Cranstroun and D. R. Pyke, Surf. Sci. **60**, 157 (1976).
- ³⁰C.-H. Nien and T. E. Madey, Surf. Sci. **380**, L527 (1996).
- ³¹T. Suzuki, Y. Temko, M. C. Xu, and K. Jacobi, Surf. Sci. **573**, 457 (2004).
- ³²F. K. Men, F. Liu, P. J. Wang, C. H. Chen, D. L. Cheng, J. L. Lin, and F. J. Himpsel, Phys. Rev. Lett. **88**, 096105 (2002).
- ³³D. M. Zehner and H. E. Farnsworth, Surf. Sci. **30**, 335 (1971).
- ³⁴E. D. Williams and N. C. Bartelt, Ultramicroscopy **31**, 36 (1989).
- ³⁵C. Herring, Phys. Rev. **82**, 87 (1951).
- ³⁶M. Drechsler and A. Müller, J. Cryst. Growth **3/4**, 518 (1968).
- ³⁷R. Kumar and H. E. Grenga, Surf. Sci. **50**, 399 (1975).
- ³⁸L. Vitos, A. V. Ruban, H. L. Skriver, and J. Kollar, Surf. Sci. **411**, 186 (1998) and reference therein.
- ³⁹D. Yu and M. Scheffler, Phys. Rev. B **70**, 155417 (2004).
- ⁴⁰H. P. Bonzel and M. Nowicki, Phys. Rev. B **70**, 245430 (2004).
- ⁴¹M. J. S. Spence, A. Hung, I. K. Snook, and I. Yarovsky, Surf. Sci. **513**, 389 (2002).
- ⁴²G. A. Wolff and J. G. Gualtieri, Am. Mineral. **47**, 562 (1962).
- ⁴³S. H. Overbury, P. A. Bertrand, and G. A. Somorjai, Chem. Rev. (Washington, D.C.) **75**, 547 (1975).
- ⁴⁴Y. S. Avraamov, A. G. Govozdev, and V. M. Kutsak, Phys. Met. Metallogr. **39**, 84 (1975).
- ⁴⁵D. A. Walko and I. K. Robinson, Phys. Rev. B **64**, 045412 (2001).
- ⁴⁶H. Wang and T. E. Madey (to be published).
- ⁴⁷C.-Z. Dong, S. M. Shivaprasad, K. J. Song, and T. E. Madey, J. Chem. Phys. **99**, 9172 (1993).
- ⁴⁸J. G. Che, C. T. Chan, C. H. Kuo, and T. C. Leung, Phys. Rev. Lett. **79**, 4230 (1997).